

PIS3R: Very Large Parallax Image Stitching via Deep 3D Reconstruction

Muhua Zhu , Xinhao Jin , Chengbo Wang , Yongcong Zhang , Yifei Xue , Tie Ji , Yizhen Lao 

Abstract—Image stitching aim to align two images taken from different viewpoints into one seamless, wider image. However, when the 3D scene contains depth variations and the camera baseline is significant, noticeable parallax occurs—meaning the relative positions of scene elements differ substantially between views. Most existing stitching methods struggle to handle such images with large parallax effectively. To address this challenge, in this paper, we propose an image stitching solution called PIS3R that is robust to very large parallax (VLP) based on the novel concept of deep 3D reconstruction. First, we apply visual geometry grounded transformer to two input images with VLP to obtain both intrinsic and extrinsic parameters, as well as the dense 3D scene reconstruction. Subsequently, we reproject reconstructed dense point cloud onto a designated reference view using the recovered camera parameters, achieving pixel-wise alignment and generating an initial stitched image. Finally, to further address potential artifacts such as holes or noise in the initial stitching, we propose a point-conditioned image diffusion module to obtain the refined result. Compared with existing methods, our solution is VLP tolerant and also provides results that fully preserve the geometric integrity of all pixels in the 3D photogrammetric context, enabling direct applicability to downstream 3D vision tasks such as SfM. Experimental results demonstrate that the proposed algorithm provides accurate stitching results for images with VLP, and outperforms the existing methods qualitatively and quantitatively.

Index Terms—Image stitching, 3D reconstruction, Diffusion model.

I. INTRODUCTION

Image stitching is a useful technique used to generate a wide field-of-view (FoV) scene by combining multiple images captured with limited FoV. It plays a vital role across various domains, including autonomous driving [9], medical imaging, surveillance, and virtual reality [10].

Most image stitching approaches follow a standard pipeline that begins by detecting and matching feature points among the

input image pair. Based on these matches, global parametric transformations—typically homographies—are estimated to warp one image onto the coordinate system of the other. The final stitched result is then obtained by blending the warped image with the reference image, particularly resolving pixel values in overlapping regions.

Image warping is a key challenge in image stitching. Homography, a widely used planar transformation model, assumes a flat scene [11]. However, in real-world scenes with depth variation and large camera baselines, this assumption fails, leading to parallax effects and noticeable misalignments—especially near object boundaries.

A. Motivations

Very large parallax (VLP). To mitigate parallax artifacts in image stitching, adaptive warping methods have been developed that divide images into grids or pixels and apply locally varying transformations [1], [2], [12]–[15]. Energy minimization frameworks further optimize these warps to reduce geometric distortion [2], [14], [15]. Some approaches employ seam-cutting techniques to align local regions and conceal misalignments in others [7], [16], [17]. However, existing smooth warping methods [1], [2], [12], [14], [15] often fail under VLP, where adjacent pixels in one image may not correspond to nearby pixels in the other view. While video-based methods using epipolar geometry have been proposed [13], they rely on temporal motion cues and are not directly applicable to still image stitching.

Downstream 3DV tasks. Almost all existing image stitching methods, including adaptive warping, seam cutting, and deep image stitching aim to seamlessly merge two input images, with visual quality as the primary criterion. However, they generally overlook whether the stitched result preserves the underlying 3D projection geometry while this geometric consistency is critical for enabling downstream 3D vision tasks such as structure-from-motion, SLAM, visual pose estimation, and depth estimation.

In summary, if we can stitch images with VLP and produce not only visually seamless result but also are capable to support downstream 3DV tasks.

TABLE I: Comparison of the proposed method PIS3R, vs. the state-of-the-art parallax-tolerate solutions.

Method	Adaptive Warping				Seam Driven		Deep Learning		PIS3R
	APAP [1] TPAMI'14	DFW [4] ICIP'17	ELA [2] TMM'18	OBJ-GSP [5] AAAI'25	PTIS [6] CVPR'14	SEAGULL [7] ECCV'16	UDIS [8] TIP'21	UDIS++ [3] ICCV'23	
Pure rotation	✓	✓	✓	✓	✓	✓	✓	✓	✓
Slight parallax	✓	✓	✓	✓	✓	✓	✓	✓	✓
Very large parallax									✓

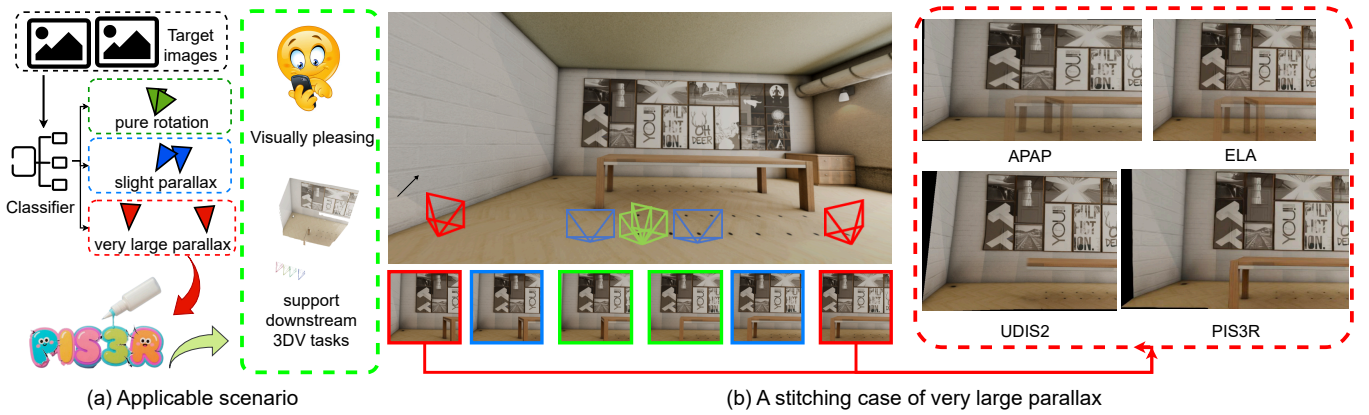


Fig. 1: PIS3R for very large parallax image stitching. (a) The image stitching task can be classified (Sec. B in Appendix) into three cases based on the baseline between target images: *pure rotation*, *slight parallax*, and *very large parallax*. In this paper, we propose a novel image stitching solution named PIS3R, specifically for stitching images with *very large parallax*. (b) Representative existing image stitching methods [1]–[3] are unable to handle stitching tasks involving *very large parallax*. Instead, our solution is achieving promising results in such challenging scenario.

B. Contribution

As shown in Fig. 2 and Tab. I, to address the limitations of existing methods under extreme parallax, we propose PIS3R, a novel image stitching framework leveraging deep 3D reconstruction for robust alignment in very large parallax (VLP) scenarios. Our method first applies the feed-forward scene reconstruction model VGGT [18] to uncalibrated image pairs, jointly recovering camera intrinsics, extrinsics, and a dense 3D scene. The reconstructed point cloud is then reprojected onto a reference view using the estimated poses, producing an initial stitched image with pixel-wise geometric alignment. A point-conditioned diffusion module further refines this result, filling holes and suppressing reprojection artifacts.

Unlike prior work that prioritizes visual seamlessness, PIS3R explicitly preserves 3D photogrammetric consistency for every pixel, enabling high-quality stitching under large parallax and ensuring compatibility with downstream 3D vision tasks like SfM, SLAM, and depth estimation. Experiments show PIS3R outperforms existing methods both qualitatively and quantitatively. Our contributions are:

- We propose a novel pipeline for stitching images with VLP based on the deep 3D reconstruction results and followed by a diffusion-based refinement, called PIS3R, which is a fundamental departure from the technical pipeline of existing methods.
- The idea of applying deep 3D reconstruction for image stitching that allows the produced results to achieve not only visually seamless alignment but also maintain 3D projection consistency, which enables our method to better support downstream 3D tasks such as SfM and SLAM over SOTAs.

II. RELATED WORK

Traditional image stitching. 1) *Adaptive warping.* Traditional stitching methods often leverage discriminative features like SIFT [19] for estimating flexible warps such as DHW [12], APAP [1], and TFA [14]. Extensions like DFW [4],

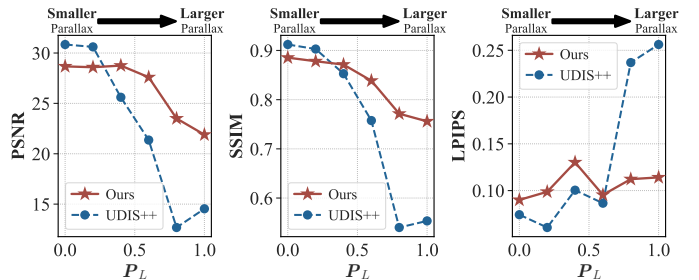


Fig. 2: The relationship between quality of stitched image and parallax variation. Our PIS3R method maintains significantly higher stability than UDIS++ across all three metrics (PSNR, SSIM, and LPIPS). As Parallax level P_L (Sec. B, Appendix) increases, stitched image quality from UDIS++ degrades substantially, whereas PIS3R demonstrates superior robustness to parallax variations. Moreover, PIS3R delivers comparable visual quality to state-of-the-art methods under pure rotation and slight parallax.

GES-GSP [20] and OBJ-GSP [5] incorporate lines, edges, mesh or semantic planes to enhance structural preservation. Furthermore, depth and planar priors have been utilized to improve alignment under challenging conditions [21], [22].

2) *Seam cutting.* Seam-cutting is commonly employed as a post-processing step for artifact reduction. Methods define energy terms based on photometric, gradient, or motion cues [23]–[25], and minimize them via graph cuts to produce visually coherent results. Seam-based alignment optimization has also been explored for minimizing stitching distortions [7], [17], [26]. **However**, these geometry-driven methods face two limitations: 1) they are sensitive to missing or weak structural features, leading to alignment failure; and 2) when geometric features are abundant, the computational overhead increases significantly.

Deep image stitching. These approaches learn high-level semantic representations from data. They have been developed

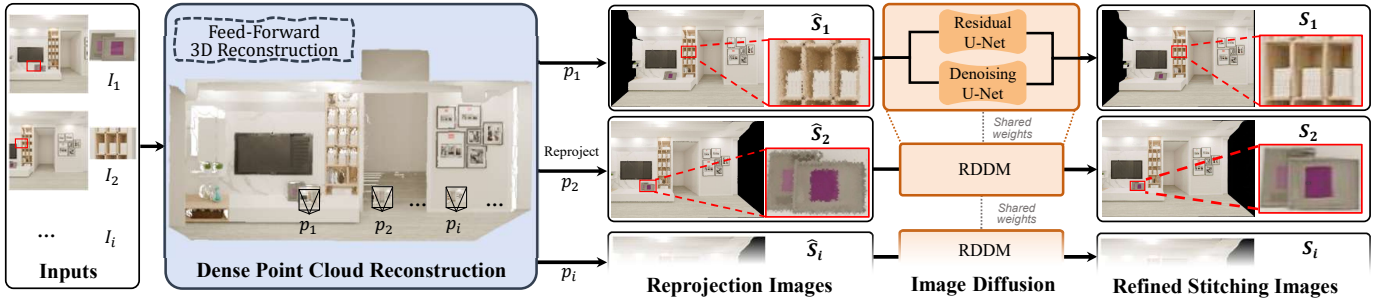


Fig. 3: Overview of the PIS3R pipeline. Given a sparse image sets, we first construct a dense point cloud representation P_w using a feed-forward deep 3D reconstruction model. Subsequently, the point cloud is reprojected onto the input camera poses p_i to generate preliminary stitching images \hat{S}_i . While these images preserve the majority of the scene’s structural information, they concurrently introduce substantial noise artifacts. To address this limitation, we train a point-conditioned denoising diffusion model to restore image fidelity, ultimately producing refined stitching images S_i .

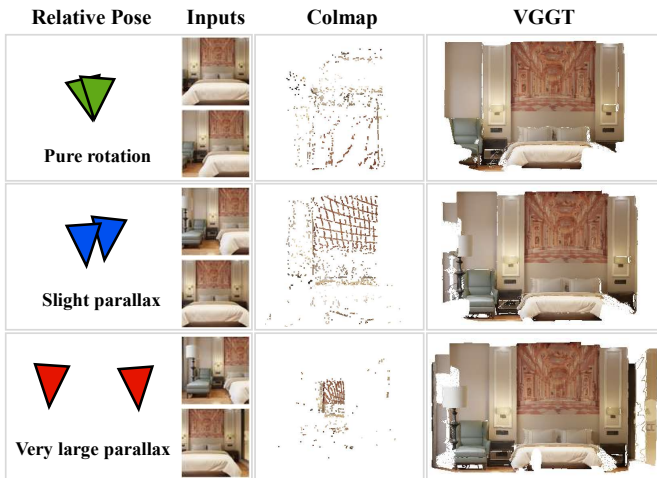


Fig. 4: Visual Comparison of 3D Reconstruction Results between COLMAP and VGGT. Reconstruction is performed under three distinct camera pose scenarios: pure rotation, slight parallax, and very large parallax. It can be observed that COLMAP produces significantly sparser point clouds across all scenarios, capturing limited structural information. In contrast, VGGT generates dense point clouds that preserve the majority of scene details.

under supervised [3], [27]–[30], weakly supervised [31], and unsupervised paradigms [32], demonstrating strong adaptability to complex scenes. Among these, unsupervised methods are particularly appealing due to the scarcity of ground truth stitched images. **However**, most of them rely on homography-based alignment, which struggles under very large parallax as shown in Fig. 2, often resulting in visible blur and artifacts in the reconstructed regions without mentioning being unable to preserve the 3D projection consistency.

III. METHODOLOGY

In this section, we start with a introduction to our image stitching framework(PIS3R). Subsequently, we provide a detailed explanation of the proposed framework and its components. Finally, we present our implementation details.

A. PIS3R Pipeline

Fig. 3 illustrates the overall architecture of our PIS3R framework. PIS3R is composed of three components as follows:

Step 1: 3D reconstruction. Given a sparse set of two or more images, we first establish their point cloud representation using a dense stereo model, as illustrated in Sec. III-B.

Step 2: Point Cloud Reprojection. Subsequently, we reproject the point cloud onto the input camera poses predicted by the dense stereo model to obtain a preliminary stitched image, as illustrated in Sec. III-C.

Step 3: Refinement of Reprojected Images. To achieve visually pleasing results while preserving the geometric structure of the scene, we train a point-conditioned image diffusion model to refine the noisy preliminary stitched image, as depicted in Sec. III-D.

B. Deep-based 3D Reconstruction

As shown in Fig. 3, we first construct a point cloud representation from the input images to obtain information about the entire scene. Certainly different from prior approaches that achieve image stitching through geometry-based 3D reconstruction, we adopt a deep-based reconstruction framework. Specifically, we employ VGGT [18]¹ to reconstruct the entire scene and estimate camera parameters simultaneously. The input consists of a sequence of RGB images capturing the same 3D scene $(I_i)_{i=1}^N \in \mathbb{R}^{H \times W \times 3}$ to corresponding 3D annotation information via a transformer, which can be described as:

$$F\left((I_i)_{i=1}^N\right) = (\mathbf{g}_i, D_i, P_i, E_i)_{i=1}^N, \quad (1)$$

where $\mathbf{g}_i \in \mathbb{R}^9$ is the camera intrinsic and extrinsic parameters, its depth map $D_i \in \mathbb{R}^{H \times W}$ and point map $P_i \in \mathbb{R}^{3 \times H \times W}$ and a grid $E_i \in \mathbb{R}^{C \times H \times W}$.

As shown in Fig. 4, we compare the point cloud representations generated by the geometry-based reconstruction framework COLMAP [33], [34]² and VGGT under three different input settings: pure rotation, slight parallax, and very large parallax. The reconstruction performance of COLMAP

¹<https://github.com/facebookresearch/vggt>

²<https://github.com/colmap/colmap>

under sparse viewpoints is predictable, while the reconstruction results of VGGT are remarkable. The quality of the point cloud and the accuracy of the predicted camera poses are crucial for image stitching using 3D reconstruction. This directly determines the geometric structure and quality of final stitched image.

C. Image Stitching via Point Cloud Reprojection

As shown in Fig. 3, to obtain the reprojected image \hat{S}_i from all input images, we first generate the transformed point cloud $P_c^i \in \mathbb{R}^{NHW \times 3}$ by converting the predicted point cloud $P_w \in \mathbb{R}^{NHW \times 3}$ from the world coordinate to the camera coordinate O_c^i using the camera extrinsic parameters (rotation R^i and translation t^i). The transformation from world coordinates to camera coordinates can be described as:

$$P_c^i = R^i P_w + t^i, \quad (2)$$

where $R^i \in \mathbb{R}^{3 \times 3}$ is the rotation matrix and $t^i \in \mathbb{R}^3$ is the translation vector for camera i . Subsequently, we reproject P_c^i onto the pixel coordinates O_{uv}^i , resulting in the pixel-wise projected points P_{uv}^i according to Eq. 3:

$$P_{uv}^i = \frac{K_i P_c^i}{Z_c^i}, \quad (3)$$

where K_i is the intrinsic matrix of camera i , and Z_c^i denotes the depth of 3D point in P_c^i .

Subsequently, we construct a pixel grid $\mathcal{P}_i \in \mathbb{R}^{H_i \times W_i \times 4}$, whose spatial resolution (H_i, W_i) is dynamically determined from the coordinate range of the projected points P_{uv}^i . For each integer pixel location (x, y) , we define the set of 3D points that project to it as Eq. 4, then we select the point with minimum depth in the camera coordinate system as Eq. 5:

$$\mathcal{N}(x, y) = \{j \mid \text{round}(P_{uv}^i(j)) = (x, y)\}. \quad (4)$$

$$k = \arg \min_{j \in \mathcal{N}(x, y)} Z_c^i(j), \quad (5)$$

$$\mathcal{P}_i(x, y) = [C_k, Z_c^i(k)],$$

where $P_w(j)$ denotes the j -th 3D point in world coordinates, $Z_c^i(j)$ is the depth of $P_w(j)$ in the i -th camera coordinate, and $P_{uv}^i(j)$ its 2D projection onto the corresponding image plane in pixel coordinates, C_j is the RGB of $P_w(j)$.

To alleviate the artifacts caused by sparse point projection while preserving valid structural voids (e.g., occlusion gaps), we propose a density-aware refinement strategy based on morphological operations. Let S_i denote the set of discrete pixel coordinates obtained from the projection:

$$S_i = \{(x, y) \in \mathbb{Z}^2 \mid \exists j : \text{round}(P_{uv}^i(j)) = (x, y)\}. \quad (6)$$

Then, we generate a valid rendering mask using morphological closing. This operation bridges small gaps between sparsely projected points without altering the global topology. We first define a binary occupancy mask M_{occ} indicating the raw projected pixels:

$$M_{\text{occ}}(x, y) = \mathbf{1}[(x, y) \in S_i]. \quad (7)$$

The geometrically closed mask, denoted as M_{closed} , is derived by applying a morphological dilation followed by an erosion with a structuring element B (e.g., a disk kernel):

$$M_{\text{closed}} = (M_{\text{occ}} \oplus B) \ominus B, \quad (8)$$

where \oplus and \ominus denote the dilation and erosion operators, respectively. We then identify the set of interior hole pixels, denoted by the mask M_{hole} , as the difference between the morphologically closed region and the original projection:

$$M_{\text{hole}}(x, y) = M_{\text{closed}}(x, y)(1 - M_{\text{occ}}(x, y)). \quad (9)$$

For any hole pixel (x, y) where $M_{\text{hole}}(x, y) = 1$, we apply an inpainting algorithm based on the Fast Marching Method (FMM) [35]. This method propagates color information from the boundary of the occupied region into the holes, effectively maintaining sharp edges and local consistency.

Finally, the refined reprojected image $\hat{S}_i \in \mathbb{R}^{H_i \times W_i \times 3}$ is composed by merging the original projection, the inpainted regions, and the background:

$$\hat{S}_i(x, y) = \begin{cases} C_i(x, y), & \text{if } M_{\text{occ}}(x, y) = 1, \\ \mathbf{H}_i(x, y), & \text{if } M_{\text{hole}}(x, y) = 1, \\ \mathbf{b}, & \text{otherwise,} \end{cases} \quad (10)$$

where $\mathbf{b} \in \mathbb{R}^3$ is a predefined background color. This formulation ensures that artifacts arising from projection sparsity are seamlessly filled, while legitimate structural voids and background regions remain preserved.

We integrate the point map with its RGB image to obtain a pose-aligned reprojected image, providing coarse 3D guidance for stitching. However, sparse inputs yield incomplete point clouds with holes and occlusions, leading to missing regions and misalignments in the reprojected image. To address this, we employ an image diffusion model to produce a visually coherent stitched result.

D. Diffusion-based Stitching Refinement

As illustrated in Fig. 3, to improve the quality of the reprojected image, our goal is to learn a conditional distribution $x \sim p(x|\hat{S})$ that generates high-quality image from the degraded reprojected image. As shown in Fig. 5 and Sec. V-D, we compared three image restoration diffusion models. Specifically, we employ **RDDM** [36] modifies to refine reprojected image \hat{S} . Different from traditional diffusion model, RDDM extends $x_T = \varepsilon$ to $x_T = x_{\text{in}} + \varepsilon$ and changes the forward diffusion process by incorporating a mixture of three terms (i.e., x_0 , x_{res} , and ε):

$$x_t = x_{t-1} + \alpha_t x_{\text{res}} + \beta_t \varepsilon_{t-1}, \quad (11)$$

$$x_t = x_0 + \bar{\alpha}_t x_{\text{res}} + \bar{\beta}_t \varepsilon_t, \quad (12)$$

where α_t and β_t are coefficients that respectively control the residual and noise injection, $\bar{\alpha}_t = \sum_{i=1}^t \alpha_i$, $\bar{\beta}_t = \sqrt{\sum_{i=1}^t \beta_i^2}$, $x_{\text{res}} = x_{\text{in}} - x_0$, and $\varepsilon \sim \mathcal{N}(0, I)$. The reverse process can be formulated as $p_\theta(x_{t-1}|x_t) := q_\sigma(x_{t-1}|x_t, x_0^\theta, x_{\text{res}}^\theta)$, where x_0^θ , x_{res}^θ are respectively predicted by a residual U-Net and a denoising U-Net. And estimated target image $x_0^\theta = x_t - \bar{\alpha}_t x_{\text{res}}^\theta - \bar{\beta}_t \varepsilon_\theta$ can be recovered according to

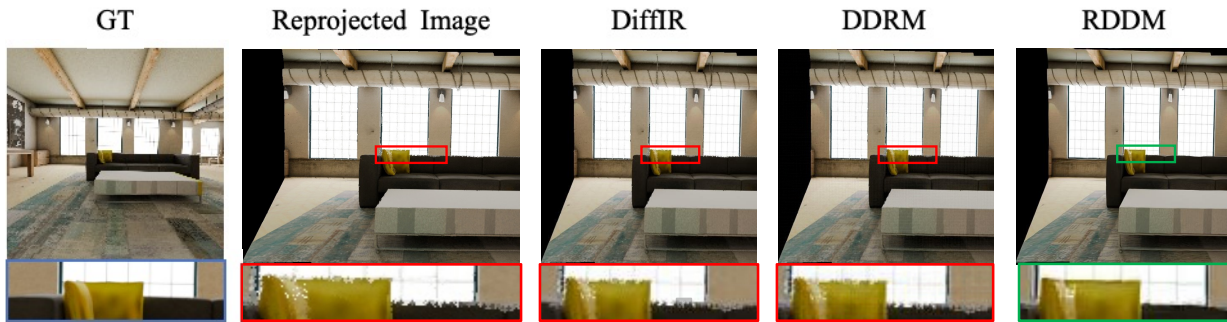


Fig. 5: Qualitative comparison of different image restoration diffusion models. We evaluated the performance of several state-of-the-art image restoration diffusion models in refining reprojected images, including *DiffIR* [37], *DDRM* [38], and *RDDM* [36].

Eq. 12. Subsequently, residual U-Net and denoising U-Net are optimized by the diffusion loss:

$$\min_{res(\theta)} = \mathbb{E} \left[\lambda_{res} \|x_{res} - x_{res}^{\theta}(x_t, t, x_{in})\|^2 \right], \quad (13)$$

$$\min_{\varepsilon(\theta)} = \mathbb{E} \left[\lambda_{\varepsilon} \|\varepsilon - \varepsilon_{\theta}(x_t, t, x_{in})\|^2 \right] \quad (14)$$

RDDM begins with residual information that captures the differences between the target and degraded images. Thus, it can effectively guide the restoration process, maximally preserve the original 3D information provided by the reprojected image, and better maintain the consistency of the geometric structure.

E. Implementation

- **3D reconstruction.** We directly use the opensource pre-trained model of VGGT to complete 3D reconstruction. To ensure the integrity of the scene information, we accept all predicted points without applying a confidence threshold.

- **Diffusion model.** To train the RDDM model, we created paired training data consisting of degraded and corresponding ground truth images. To better suit our task, we manually processed ground truth images from the **RainDrop** dataset [39] to generate the customized 3DIS-D dataset, incorporating various noises for enhanced robustness beyond reprojection artifacts and occlusions.

We adopted a progressive training strategy with a global learning rate of $8e^{-5}$ and batch size of 1. In the first stage, we trained on 3DIS-D at 512×512 resolution with 10 sampling steps for 120,000 iterations, using ground truth as targets and processed images as degraded inputs. In the second stage, we fine-tuned on **GoPro** [40] dataset at the same resolution with 5 sampling steps for 20,000 iterations. Notably, our approach achieves satisfactory results with limited training data. All training and testing were performed on an NVIDIA RTX 4090 GPU.

IV. DISCUSSION

- **Is PIS3R suitable for pure rotation or slight parallax?** PIS3R delivers comparable visual quality to state-of-the-art methods under pure rotation or slight parallax (Fig. 10) but requires more processing time per image than UDIS++ (Tab. VII). We recommend PIS3R for scenarios with large

parallax and propose a parallax classifier (Sec. B, Appendix) to estimate input image parallax levels.

- **Why deep 3DR?** Deep 3DR solutions such as VGGT demonstrate significantly greater robustness and accuracy than classical SfM like COLMAP in estimating camera intrinsic and extrinsic parameters, particularly in challenging two-view scenarios such as pure rotation and VLP (as shown in Fig. 1 and detailed in the Sup material). Moreover, the point maps predicted by VGGT offer substantially higher density compared to traditional SfM point clouds, providing strong support for the following image stitching reprojection step.

- **Why PIS3R is geometry-preserve?** PIS3R employs a deep-based reconstruction framework to accurately predict the point cloud representation and the camera intrinsic and extrinsic parameters. Accurate pose estimation of the images is fundamental to preserving geometric structure in PIS3R. This is also the reason why SOTA methods fail to maintain geometric structure. As illustrated in Sec. V-C and tab. IV.

- **How does PIS3R support 3D vision downstream tasks?** Our preliminary stitched image is generated via reprojection based on the camera parameters. This provides the stitched image with accurate geometric spatial information. As shown in Fig. 6 and Sec. V-C, stitching results of PIS3R in VLP scenarios can be directly input into a geometry-based 3D reconstruction framework for point cloud reconstruction, while better maintaining the geometric structure and integrity of the scene due to its excellent geometry preservation capability.

- **Limitation?** PIS3R, while effective in many scenarios, is not without limitations. As with most SOTA image stitching approaches, certain constraints must be acknowledged:

- **Extremely large parallax and rotation:** When both large parallax and considerable rotation are present in the input images, non-overlapping areas in either the foreground or background during the reprojection process may lead to pronounced missing regions and distortions.
- **Large-area object occlusion:** When the occluded area of the background is large, the missing regions in the reprojected image lack detailed geometric structure. This effectively disables the residual diffusion process in those areas, leading to pure noise generation, which results in distortions, inconsistencies, and holes.

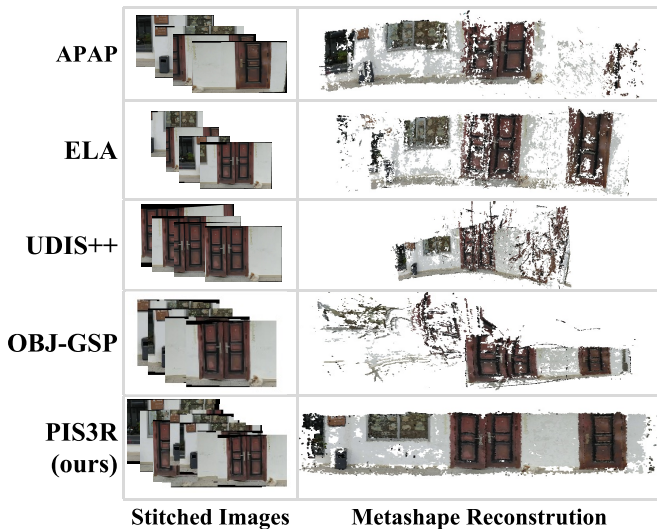


Fig. 6: The results of MetaShape reconstruction using stitched images. When used as inputs for 3D reconstruction in MetaShape, images stitched with APAP and ELA resulted in large number of surface holes. Images stitched with UDIS++ and OBJ-GSP exhibited significant distortions to geometric structure. In contrast, reconstructions generated from our stitched images consistently exhibited high geometric consistency and completeness within MetaShape. This enhanced structural integrity suggests that PIS3R is more suitable for downstream 3D reconstruction tasks.

V. EXPERIMENTS

In this section, we conduct a comprehensive series of comparative experiments to evaluate the performance of our method PIS3R. We compare PIS3R against three state-of-the-art image stitching solutions: **APAP** [1], **ELA** [2], **UDIS++** [3] and **OBJ-GSP** [5].

A. Datasets

PIS3R proposes a solution for image stitching under very large parallax (VLP)—a scenario not adequately addressed by existing datasets. To evaluate its effectiveness, we introduce a self-collected large-parallax dataset comprising both synthetic and real image pairs. Furthermore, to demonstrate its applicability under slight parallax, we also evaluate our method on the UDIS-D [8] dataset.

1) *UDIS-D Dataset*: UDIS-D is a large-scale image dataset designed for image stitching or image registration. It includes image pairs with varying overlap ratios, different levels of parallax, and diverse scenarios such as indoor, outdoor, nighttime, low-light, snowy conditions, and zoom variations.

2) *Synthetic Dataset*: As shown in Fig. 7a, this test dataset was rendered using Blender. It comprises 20 distinct scenes ^{3 4 5} with 600 image pairs and their corresponding ground truth (GT) images. Most image pairs have large-baseline, large-parallax characteristics.

³<https://sketchfab.com>

⁴<https://blenderco.cn/>

⁵<https://free3d.com/zh/3d-models/blender>

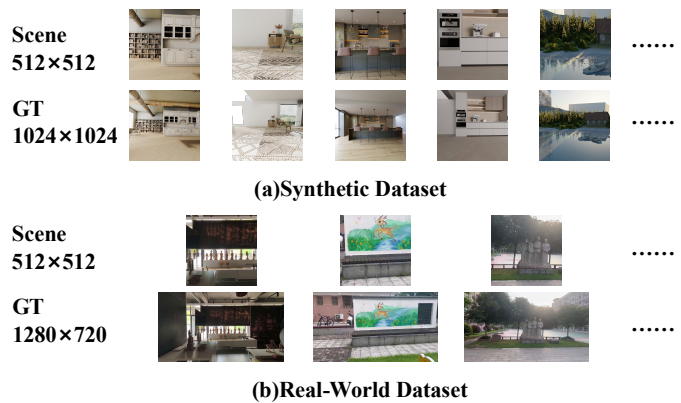


Fig. 7: Sample images from the experimental dataset. (a) Synthetic dataset rendered by Blender [41]. (b) Real-world dataset captured by ourselves. Additionally, each scene image and its ground-truth image share the same camera extrinsic.

3) *Real-World Dataset*: As shown in Fig. 7b, we capture the dataset with a mobile phone. It comprises 10 distinct scenes with 682 image pairs and their corresponding GT images. We test this real-world dataset to validate the performance of PIS3R in real-world scenarios.

B. Comparison of Image Stitching

1) *Evaluation Metrics*: We employ two sets of evaluation metrics for different datasets.

• *On Dataset with GT*. The traditional image stitching paradigm consists of warping and composition stages. However, as a 3D-reconstruction-based image stitching paradigm, PIS3R does not include these steps. Therefore, overlapping regions based metrics of warping results is not suitable for PIS3R. Notably, each reference image shares the same camera extrinsics with its GT image (Fig. 7), and scene images are obtained by center-cropping GT images. Theoretically, stitched images should share the same extrinsics with reference images. Thus, we propose a novel three-step metric computation approach (Fig.4 in Appendix):

Step 1: Padding. Firstly, we pad the reference image to match the size of the GT image.

Step 2: Registration. Subsequently, we register the stitched image to the padded reference image.

Step 3: Compute metrics. Then we can compute metrics for the valid pixels between the registered stitched image and the GT image.

We employ metrics including: **PSNR**, **SSIM** [42], **LPIPS** [43]. Furthermore, to avoid metric inaccuracies caused by registration failures, we calculated the Registration Success Rate (**RSR**):

$$RSR = (1 - \frac{R_f}{n}) \times 100\%, \quad (15)$$

where n is the total image pairs in dataset, R_f is the number of failed registration cases. Subsequently, we recomputed the metrics excluding the registration failed cases.

• *On Dataset without GT*. Following the evaluation protocol of recent state-of-the-art methods OBJ-GSP, we

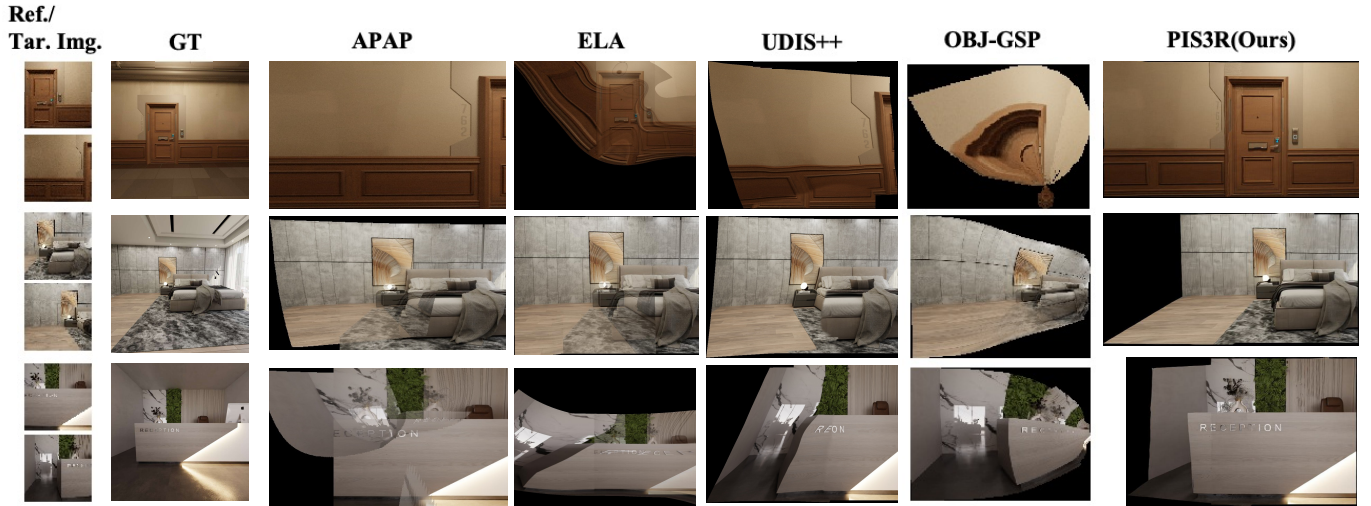


Fig. 8: Qualitative comparison of stitched images on synthetic dataset. Our PIS3R generates images with significantly more complete structures and fewer severe distortions compared to existing image stitching algorithms APAP, ELA, OBJ-GSP and UDIS++ in both datasets. Ref./Tar. Img. refers to Reference and Target Images.

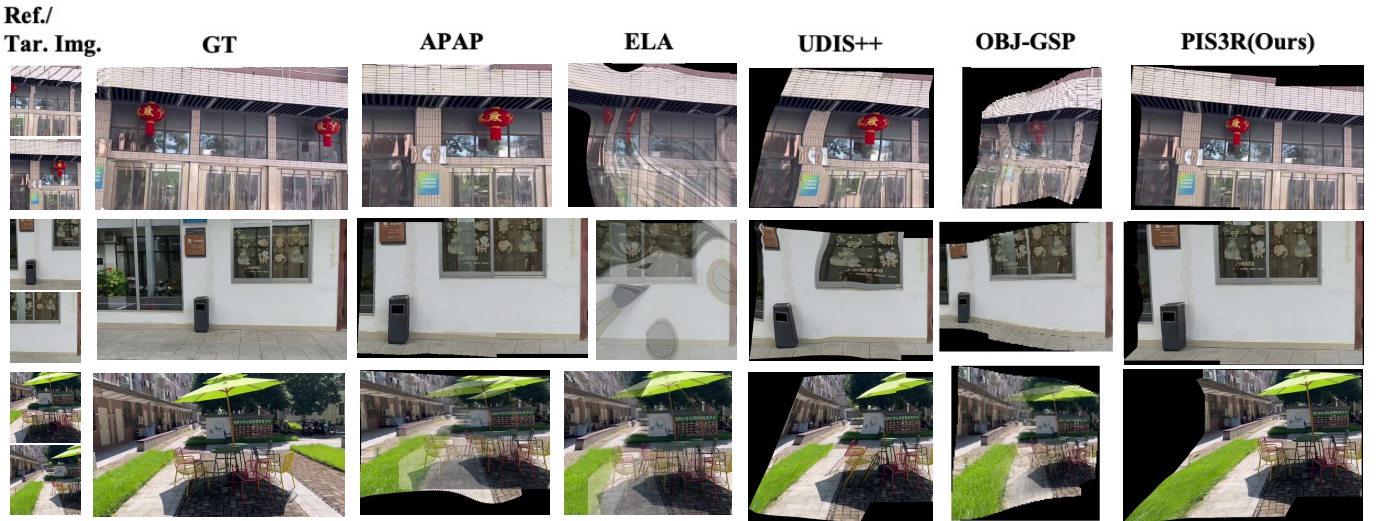


Fig. 9: Qualitative comparison of stitched images on real-world dataset. Our PIS3R generates images with significantly more complete structures and fewer severe distortions compared to existing image stitching algorithms APAP, ELA, OBJ-GSP and UDIS++ in both datasets. Ref./Tar. Img. refers to Reference and Target Images.

adopt the Naturalness Image Quality Evaluator(NIQE) [44] and Perception based Image Quality Evaluator(PIQE) [45].

2) *Image Stitching in Synthetic Dataset:* We first evaluate four different methods on our custom synthetic dataset.

- *Qualitative Comparison.* The qualitative comparison results are shown in Fig. 8, where the reference and target images are displayed in the left-most column. APAP, ELA, OBJ-GSP and UDIS++ exhibit noticeable artifacts and geometric inconsistencies, while Our results better preserve the geometric structure of the scene. Additional cases are provided in Fig. 1 of Appendix.

- *Quantitative Comparison.* The quantitative comparison results are presented in Tab. II. Our PIS3R outperforms the other three methods across all metrics when including all

data in the calculations. We still maintain a substantial lead in PSNR, SSIM after excluding failed registration cases. What is noteworthy is that **RSR** substantially indicates the method’s ability to maintain geometric consistency.

3) *Image Stitching in Real-World Dataset:* We employ a real-world dataset captured by ourselves to validate the performance of PIS3R in real-world scenarios.

- *Qualitative Comparison.* The qualitative comparison results are presented in Fig. 9. APAP, ELA, OBJ-GSP and UDIS++ exhibit noticeable artifacts and geometric inconsistencies. In contrast, our PIS3R method consistently generates images with significantly more complete structures and fewer severe distortions in these complex and challenging scenarios. Additional cases are provided in Fig. 2 of Appendix.

Dataset	Method	All Image Pairs				W/O Failed Registration Cases		
		PSNR \uparrow	SSIM \uparrow	LPIPS \downarrow	RSR \uparrow	PSNR \uparrow	SSIM \uparrow	LPIPS \downarrow
Synthetic Dataset	APAP	19.116	0.659	0.169	87.5%	20.063	0.691	0.146
	ELA	19.813	0.670	0.158	91.5%	20.487	0.719	0.139
	UDIS++	19.858	0.690	0.139	86.2%	21.038	0.748	0.097
	OBJ-GSP	16.961	0.538	0.205	82.3%	17.6733	0.563	0.1846
	PIS3R	22.026	0.782	0.110	95.7%	22.351	0.796	0.102
Real World Dataset	APAP	16.764	0.525	0.246	81.6%	18.047	0.572	0.207
	ELA	16.983	0.547	0.245	98.2%	17.064	0.553	0.242
	UDIS++	17.390	0.554	0.204	90.3%	18.874	0.615	0.208
	OBJ-GSP	15.3099	0.3918	0.2744	73.89%	15.9051	0.4123	0.2495
	PIS3R	19.674	0.644	0.180	100.0%	19.674	0.644	0.180

TABLE II: Quantitative comparison of image stitching on synthetic dataset and real world dataset. PIS3R outperforms the other three methods across PSNR, SSIM and LPIPS when all image pairs are included in the evaluation. Moreover, even after excluding registration-failed cases, PIS3R still maintains a noticeable advantage in PSNR and SSIM.

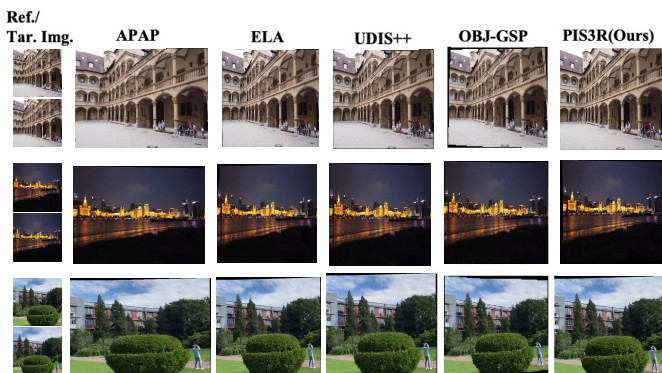


Fig. 10: Qualitative comparison of stitched images on UDIS-D dataset. Even without training on the UDIS-D dataset, PIS3R remains visually comparable to various state-of-the-art methods.

Dataset	Method	PIQE \downarrow	NIQE \downarrow
UDIS-D	APAP	44.58	4.383
	ELA	47.87	4.152
	UDIS++	43.79	4.098
	OBJ-GSP	56.96	4.885
	PIS3R	44.13	4.059

TABLE III: Quantitative comparison of image stitching on the UDIS-D [8] dataset. PIS3R performs comparably to UDIS++ and both outperform other methods.

- Quantitative Comparison. As shown in Tab. II, PIS3R demonstrates superior performance across all evaluation metrics on the complete real-world dataset. Moreover, after excluding failed registration cases, it continues to achieve leading performance on all metrics.

4) *Image Stitching in UDIS-D Dataset:* We evaluate PIS3R on the UDIS-D dataset, which primarily involves pure rotation and slight parallax.

- Qualitative Comparison. The qualitative comparison results are presented in Fig. 10. Even without training on the UDIS-D dataset, PIS3R remains visually comparable to various state-of-the-art methods.
- Quantitative Comparison. As shown in Tab. III, PIS3R

performs comparably to UDIS++ and outperform APAP, ELA and OBJ-GSP, even without training on the UDIS-D dataset.

C. Geometric Consistency Verification of Stitched Images

In this section, we perform geometric consistency verification on stitched images of synthetic dataset to ensure structural accuracy.

- Evaluation Metric. Since the camera parameters of the images in Blender are available, we evaluated Geometric Consistency by computing the Sampson Epipolar Error (d_{sam}^2) on two stitched images:

$$d_{Sam}^2 = \frac{(x_2^T F x_1)^2}{(F x_1)_1^2 + (F x_1)_2^2 + (F^T x_2)_1^2 + (F^T x_2)_2^2}, \quad (16)$$

where F is fundamental matrix, x_1 and x_2 respectively denote the homogeneous coordinates of a pair of corresponding feature points detected in the first and second images.

- Qualitative Comparison. As shown in Fig. 6, we fed the stitched images of each method into AgiSoft MetaShape [46] for reconstruction. PIS3R’s stitching results in VLP scenarios can be directly input into a Structure From Motion (sfm) framework for point cloud reconstruction, while better maintaining the geometric structure and integrity of the scene due to its excellent geometry preservation capability.

- Quantitative Comparison. As shown in Table IV, PIS3R achieves a significantly lower epipolar error for stitched images exhibiting VLP conditions, notably outperforming the other three approaches.

	APAP	ELA	UDIS++	OBJ-GSP	PIS3R
d_{Sam}^2 (pixel) \downarrow	22.78	38.97	12.94	16.43	4.12

TABLE IV: Sampson epipolar error of stitching image on synthetic dataset. PIS3R achieves a lower epipolar error for stitched images exhibiting very large parallax conditions.

D. Ablation studies

1) *Comparison of Different 3D Reconstruction Models:* We compare three feed-forward deep 3D reconstruction models: Dust3R [48], VGGT [18], and Mast3R [47].

Dataset	Model	All image pairs		
		PSNR \uparrow	SSIM \uparrow	LPIPS \downarrow
Synthetic Dataset	Dust3R	21.872	0.769	0.134
	Mast3R	21.814	0.780	0.126
	VGGT	22.754	0.794	0.121
Real World Dataset	Dust3R	18.134	0.617	0.239
	Mast3R	18.965	0.636	0.221
	VGGT	20.134	0.652	0.207

TABLE V: Ablation studies of feed-back deep 3D reconstruction models on synthetic and real world dataset. We compare the quality of reprojected images without refine. VGGT achieves the best reprojection results in our task.

Dataset	Model	All image pairs		
		PSNR \uparrow	SSIM \uparrow	LPIPS \downarrow
Synthetic Dataset	w/o Refine	22.754	0.794	0.121
	DiffIR	21.361	0.740	0.120
	DDRM	20.894	0.706	0.132
	RDDM	22.026	0.782	0.110
Real World Dataset	w/o Refine	20.134	0.652	0.207
	DiffIR	18.744	0.624	0.193
	DDRM	18.697	0.616	0.210
	RDDM	19.674	0.644	0.180

TABLE VI: Ablation studies of diffusion models on synthetic and real world dataset. Refining with RDDM improves the perceptual quality of the stitched images (as measured by LPIPS), while having only a negligible impact on pixel-level fidelity metrics such as PSNR and SSIM.

- Qualitative Comparison. As shown in Fig. 5, VGGT demonstrates visually superior reconstruction results.
- Quantitative Comparison. As shown in Tab. V, we compare the quality of reprojected images without refinement. VGGT achieves the best reprojection results in our task

2) *Comparison of Different Diffusion Models:* We compared three image restoration diffusion models: DiffIR [37]⁶, DDRM [38]⁷, and RDDM [36]⁸. We train DiffIR and RDDM on 3DIS-D dataset (as illustrated in Sec. III-E) and present comparative results of the restoration performance. Notably, DDRM does not rely on task-specific training and can be applied directly. RDDM can effectively remove noise while

⁶<https://github.com/Zj-BinXia/DiffIR>

⁷<https://github.com/bahjat-kawar/ddrm>

⁸<https://github.com/nachifur/RDDM>



Fig. 11: Qualitative comparison of different feed-back deep 3D reconstruction models including VGGT [18], MAST3R [47] and DUST3R [48]. VGGT demonstrates visually superior reconstruction results.

preserving geometric structures.

- Qualitative Comparison. As shown in Fig. 5, RDDM demonstrates excellent optimization results due to its unique diffusion mechanism.

- Quantitative Comparison. As shown in Tab. VI, we quantify the metric differences between reprojected images processed and unprocessed by the diffusion model. Refining with RDDM improves the perceptual quality of the stitched images, while having only a negligible impact on pixel-level fidelity metrics such as PSNR and SSIM. This trade-off is thus deemed both acceptable and necessary.

E. Running time

	APAP ¹	ELA ¹	UDIS++ ²	OBJ-GSP ¹	PIS3R ²
Time(s) \downarrow	1.2	6.1	2.7	1.6	5.8

TABLE VII: Runtime of PIS3R on image stitching. 1: tested with Intel i9-14900KF 3.20GHZ CPU; 2: tested with NVIDIA RTX 4090 GPU.

As shown in Tab. VII, since we do not have the warp and composition steps, we compare the average time required to stitch a complete image, excluding the time spent loading the model. PIS3R takes 5.8 seconds to stitch an image, including 1.1 seconds for reconstruction, 3.5 seconds for reprojection, and 1.2 seconds for diffusion model refinement.

VI. CONCLUSION

We proposed PIS3R, a very large parallax-tolerant image stitching framework based on deep 3D reconstruction. By estimating camera parameters and reconstructing a dense point cloud via a visual geometry-grounded transformer, our method achieves pixel-wise alignment through reprojection. A point-conditioned image diffusion module further refines the result. Unlike existing methods, PIS3R preserves 3D geometric consistency, enabling seamless stitching and compatibility with downstream 3D tasks. Experimental results show that PIS3R outperforms prior approaches both visually and quantitatively under very large parallax.

REFERENCES

- [1] J. Zaragoza, T.-J. Chin, Q.-H. Tran, M. S. Brown, and D. Suter, “As-projective-as-possible image stitching with moving dlt,” *TPAMI*, vol. 36, no. 7, pp. 1285–1298, 2014.
- [2] J. Li, Z. Wang, S.-H. Lai, Y. Zhai, and M. Zhang, “Parallax-tolerant image stitching based on robust elastic warping,” *IEEE Transactions on Multimedia*, vol. 20, no. 7, pp. 1672–1687, 2018.
- [3] W. Nie, Y. Zhang, J. Zhu, Y. Wang, Y. Chen, and Y. Fang, “Parallax-tolerant unsupervised deep image stitching,” in *Proceedings of the IEEE/CVF International Conference on Computer Vision (ICCV)*, 2023.
- [4] X. Li, Y. Zhao, H. Lu, and R. Wang, “Dual-feature warping based robust image stitching,” in *ICIP*, 2017, pp. 2394–2398.
- [5] W. Cai and W. Yang, “Object-level geometric structure preserving for natural image stitching,” in *Proceedings of the AAAI Conference on Artificial Intelligence*, vol. 39, no. 2, 2025, pp. 1926–1934.
- [6] F. Zhang and F. Liu, “Parallax-tolerant image stitching,” in *Proceedings of the IEEE Conference on Computer Vision and Pattern Recognition (CVPR)*, June 2014.
- [7] K. Lin, N. Jiang, L.-F. Cheong, M. N. Do, and J. Lu, “Seagull: Seam-guided local alignment for parallax-tolerant image stitching,” in *ECCV*, 2016, pp. 370–385.

- [8] L. Nie, C. Lin, K. Liao, S. Liu, and Y. Zhao, "Unsupervised deep image stitching: Reconstructing stitched features to images," *IEEE Transactions on Image Processing*, vol. 30, pp. 6184–6197, 2021.
- [9] C. Kinzig, I. Cortés, C. Fernández, and M. Lauer, "Real-time seamless image stitching in autonomous driving," in *2022 25th International Conference on Information Fusion (FUSION)*. IEEE, 2022, pp. 1–8.
- [10] R. Anderson, D. Gallup, J. T. Barron, J. Kontkanen, N. Snavely, C. Hernández, S. Agarwal, and S. M. Seitz, "Jump: virtual reality video," *ACM transactions on graphics (TOG)*, vol. 35, no. 6, pp. 1–13, 2016.
- [11] R. Hartley and A. Zisserman, *Multiple View Geometry in Computer Vision*. Cambridge University Press, 2003.
- [12] J. Gao, S. Kim, and M. S. Brown, "Constructing image panoramas using dual-homography warping," in *CVPR*, 2011, pp. 49–56.
- [13] K.-Y. Lee and J.-Y. Sim, "Stitching for multi-view videos with large parallax based on adaptive pixel warping," *IEEE Access*, vol. 6, pp. 26 904–26 917, 2018.
- [14] W. Lin, S. Liu, Y. Matsushita, T.-T. Ng, and L.-F. Cheong, "Smoothly varying affine stitching," in *CVPR*, 2011, pp. 345–352.
- [15] G. Zhang, Y. He, W. Chen, J. Jia, and H. Bao, "Multi-viewpoint panorama construction with wide-baseline images," *IEEE Transactions on Image Processing*, vol. 25, no. 7, pp. 3099–3111, 2016.
- [16] J. Gao, Y. Li, T.-J. Chin, and M. S. Brown, "Seam-driven image stitching," in *Proceedings of the Eurographics (EG)*, 2013.
- [17] F. Zhang and F. Liu, "Parallax-tolerant image stitching," in *CVPR*, 2014, pp. 3262–3269.
- [18] J. Wang, M. Chen, N. Karaev, A. Vedaldi, C. Rupprecht, and D. Novotny, "Vggt: Visual geometry grounded transformer," in *Proceedings of the Computer Vision and Pattern Recognition Conference*, 2025, pp. 5294–5306.
- [19] D. G. Lowe, "Distinctive image features from scale-invariant keypoints," *International journal of computer vision*, vol. 60, no. 2, pp. 91–110, 2004.
- [20] K. Lin, J. Lu, J. Zhou, and Z. Zheng, "Ges-gsp: Geometrically and semantically consistent image stitching via grid-based spatial partitioning," *IEEE Transactions on Image Processing*, vol. 30, pp. 2115–2128, 2021.
- [21] Y. Liu, J. Yang, T. Zhu, J. Fu, and J. Luo, "Attentional semantic alignment for panorama image stitching," in *ECCV*, 2020, pp. 128–144.
- [22] T. Zhou, X. Zhang, H. Bao, and G. Zhang, "Stereo-aware multi-projective warping for panoramic image stitching," in *ECCV*, 2018, pp. 21–36.
- [23] V. Kwatra, A. Schodl, I. Essa, G. Turk, and A. Bobick, "Graphcut textures: Image and video synthesis using graph cuts," in *SIGGRAPH*, 2003, pp. 277–286.
- [24] A. Agarwala, M. Agrawala, M. Cohen, B. Curless, D. Salesin, and R. Szeliski, "Interactive digital photomontage," in *ACM Transactions on Graphics (TOG)*, vol. 23, no. 3, 2004, pp. 294–302.
- [25] L. Bao, J. Sun, and Q. Yang, "Fast edge-preserving patchmatch for large displacement optical flow," *IEEE Transactions on Image Processing*, vol. 22, no. 12, pp. 5004–5017, 2013.
- [26] T. Zhou, G. Zhang, and H. Bao, "Stitchability determination for image stitching," in *ECCV*, 2018, pp. 162–177.
- [27] Z. Lin, X. Xu, Z. Liu, and W. Wei, "Deep image stitching via exploring semantic cues," in *ACM Multimedia*, 2021, pp. 1234–1242.
- [28] T. Zhou, G. Zhang, and H. Bao, "Learning multi-homography alignment with attention for panoramic image stitching," in *CVPR*, 2022, pp. 1324–1333.
- [29] W. Huang, K. Wang, and J. Fu, "Image stitching with transformer," in *ACCV*, 2021.
- [30] T. Zhou, M. Liu, G. Zhang, and H. Bao, "Warpstitch: Learning topology-aware warping for image stitching," in *ECCV*, 2022, pp. 670–687.
- [31] W. Nie, Y. Zhang, and Y. Fang, "Unsupervised image stitching with deep homography alignment and local refinement," in *Proceedings of the IEEE International Conference on Multimedia and Expo (ICME)*, 2022.
- [32] —, "Unsupervised deep homography for parallax-robust image stitching," in *ICIP*, 2021, pp. 3153–3157.
- [33] J. L. Schönberger, E. Zheng, M. Pollefeys, and J.-M. Frahm, "Pixel-wise view selection for unstructured multi-view stereo," in *European Conference on Computer Vision (ECCV)*, 2016.
- [34] J. L. Schönberger and J.-M. Frahm, "Structure-from-motion revisited," in *Conference on Computer Vision and Pattern Recognition (CVPR)*, 2016.
- [35] A. Telea, "An image inpainting technique based on the fast marching method," *Journal of graphics tools*, vol. 9, no. 1, pp. 23–34, 2004.
- [36] J. Liu, Q. Wang, H. Fan, Y. Wang, Y. Tang, and L. Qu, "Residual denoising diffusion models," in *Proceedings of the IEEE/CVF Conference on Computer Vision and Pattern Recognition*, 2024, pp. 2773–2783.
- [37] B. Xia, Y. Zhang, S. Wang, Y. Wang, X. Wu, Y. Tian, W. Yang, and L. Van Gool, "Diffir: Efficient diffusion model for image restoration," in *Proceedings of the IEEE/CVF international conference on computer vision*, 2023, pp. 13 095–13 105.
- [38] B. Kawar, M. Elad, S. Ermon, and J. Song, "Denoising diffusion restoration models," *Advances in neural information processing systems*, vol. 35, pp. 23 593–23 606, 2022.
- [39] R. Qian, R. T. Tan, W. Yang, J. Su, and J. Liu, "Attentive generative adversarial network for raindrop removal from a single image," in *Proceedings of the IEEE conference on computer vision and pattern recognition*, 2018, pp. 2482–2491.
- [40] S. Nah, T. Hyun Kim, and K. Mu Lee, "Deep multi-scale convolutional neural network for dynamic scene deblurring," in *Proceedings of the IEEE conference on computer vision and pattern recognition*, 2017, pp. 3883–3891.
- [41] B. O. Community, *Blender - a 3D modelling and rendering package*. Blender Foundation, Stichting Blender Foundation, Amsterdam, 2018. [Online]. Available: <http://www.blender.org>
- [42] Z. Wang, A. C. Bovik, H. R. Sheikh, and E. P. Simoncelli, "Image quality assessment: from error visibility to structural similarity," *IEEE transactions on image processing*, vol. 13, no. 4, pp. 600–612, 2004.
- [43] R. Zhang, P. Isola, A. A. Efros, E. Shechtman, and O. Wang, "The unreasonable effectiveness of deep features as a perceptual metric," in *Proceedings of the IEEE conference on computer vision and pattern recognition*, 2018, pp. 586–595.
- [44] A. Mittal, R. Soundararajan, and A. C. Bovik, "Making a "completely blind" image quality analyzer," *IEEE Signal processing letters*, vol. 20, no. 3, pp. 209–212, 2012.
- [45] N. Venkatanath, D. Praneeth, S. C. Sumohana, S. M. Swarup *et al.*, "Blind image quality evaluation using perception based features," in *2015 twenty first national conference on communications (NCC)*. IEEE, 2015, pp. 1–6.
- [46] Agisoft LLC, "Agisoft metashape - professional photogrammetry software," <https://www.agisoft.com/>, 2023, accessed: [2025-1-15].
- [47] V. Leroy, Y. Cabon, and J. Revaud, "Grounding image matching in 3d with mast3r," in *European Conference on Computer Vision*. Springer, 2024, pp. 71–91.
- [48] S. Wang, V. Leroy, Y. Cabon, B. Chidlovskii, and J. Revaud, "Dust3r: Geometric 3d vision made easy," in *Proceedings of the IEEE/CVF Conference on Computer Vision and Pattern Recognition*, 2024, pp. 20 697–20 709.